Polycrystal Simulations Investigating the Effect of Additional Slip System Availability in a 6063 Aluminum Alloy at Elevated Temperature

Antoinette M. Maniatty[1]
e-mail: maniaa@rpi.edu

David J. Littlewood

Jing Lu[2]

Department of Mechanical, Aerospace, and Nuclear Engineering,
Rensselaer Polytechnic Institute,
110 8th Street,
Troy, NY 12180

In order to better understand and predict the intragrain heterogeneous deformation in a 6063 aluminum alloy deformed at an elevated temperature, when additional slip systems beyond the usual octahedral slip systems are active, a modeling framework for analyzing representative polycrystals under these conditions is presented. A model polycrystal that has a similar microstructure to that observed in the material under consideration is modeled with a finite element analysis. A large number of elements per grain (more than 1000) are used to capture well the intragranular heterogeneous response. The polycrystal model is analyzed with three different sets of initial orientations. A compression test is used to calibrate the material model, and a macroscale simulation of the compression test is used to define the deformation history applied to the model polycrystal. In order to reduce boundary condition effects, periodic boundary conditions are applied to the model polycrystal. To investigate the effect of additional slip systems expected to be active at elevated temperatures, the results considering only the 12 {111}⟨110⟩ slip systems are compared to the results with the additional 12 {110}⟨110⟩ and {001}⟨110⟩ slip systems available (i.e., 24 available slip systems). The resulting predicted grain structure and texture are compared to the experimentally observed grain structure and texture in the 6063 aluminum alloy compression sample as well as to the available data in the literature, and the intragranular misorientations are studied. [DOI: 10.1115/1.2884338]

1 Introduction

A better understanding of the relationship between processing and product properties can help to improve the performance of aluminum alloys. The macroscale properties that influence performance, such as formability, yield strength, and anisotropy, are largely dictated by microstructural features including grain shape, grain size, and orientation and misorientation distributions, which are formed during the metal forming process (see Olaf and Hirsch [1] for a review).

Grains distort and rotate to accommodate deformation. The level of stretching and rotation during deformation is related to the amount of slip along crystallographic slip systems within the grain, which, in turn, is related to dislocation motion. The rotational component of the deformation tends to cause grains to rotate toward preferred crystallographic orientations, depending on the nature of the deformation, resulting in a pattern of crystallographic orientations referred to as the texture.

The joint requirements of compatibility and stress equilibrium at grain boundaries lead to nonuniform slip system activity and rotation within individual grains. This leads to the division of crystals into regions of differing lattice orientation. Bay et al. [2] observed that dislocation boundaries separate regions of a grain that have differing orientations resulting from nonuniform deformation in cold worked face-centered cubic metals. Furthermore, they found that the number of active slip systems in these regions was frequently less than that required to fulfill the Taylor criterion [3] (i.e., five active slip systems assuming uniform strain within each grain of a polycrystal). The same observation was made earlier by Fleischer [4], who counted the number of active slip systems in deformed polycrystalline brass in grains fully constrained by neighboring crystals. Fleischer found that approximately 40% of the grains had less than five active slip systems due to the nonuniform deformation within the grains. One reason for this is that at room temperature the strain rate sensitivity is very low leading to the deformation being mostly concentrated in localized regions of high slip, as shown in Peirce et al. [5]. Hughes et al. [6–8] studied the misorientations, i.e., the minimum relative angle that reflects crystal symmetry, that developed between the different regions of the grains and the dislocation boundaries that separated these regions as a result of nonuniform lattice rotation within the grains. They found that the misorientation distribution, for both incidental dislocation boundaries and geometrically necessary boundaries, scaled with the average misorientation angle, and the average misorientation angle, for both types of subgrain boundaries, scaled with the effective strain. The present work investigates, through simulation, the effect that additional active slip systems at elevated temperatures may have on intragranular misorientations.

The deformation microstructure (prior to heat treatments) that results at elevated temperatures and high strain rates, typical in industrial forming processes, shows some key differences to that observed in cold working. First, because the rate sensitivity is higher at elevated temperatures, the deformation is more diffused. Second, at room temperature, only the 12 octahedral slip systems {111}⟨110⟩ are active, whereas at elevated temperatures (above a homologous temperature of 0.65), additional slip systems have been observed to be active (see, for example, Perocheau and Driver [9], Kvapilova and Orlova [10], and Martin and Caillard

[1]Corresponding author.
[2]Present address: Wellstream International, Houston, TX.

Contributed by the Materials Division of ASME for publication in the JOURNAL OF ENGINEERING MATERIALS AND TECHNOLOGY. Manuscript received August 1, 2007; final manuscript received January 25, 2008; published online March 19, 2008. Assoc. Editor: Matthew P. Miller.

[11]). Maurice and Driver [12], Perocheau and Driver [9], and Ringeval et al. [13] investigated pure aluminum as well as Al–1%Mn, Al–1%Mn–1%Mg systems (3XXX alloys, solid solution), and an Al–3Mg–Sc(Zr) alloy. They found similar slip behavior in each of these systems, with slip confirmed on {110} and {001} planes as well as sometimes on the {112} planes based on the observed texture components and slip trace analysis. Stout et al. [14] did a detailed study of the texture that developed in a 5182 aluminum magnesium manganese alloy deformed in uniaxial compression at elevated temperatures. In that work, they investigated the texture developed for deformations over a range of temperatures between room temperature and 550°C. Below 300°C, the usual ⟨110⟩ compression texture developed, i.e., the ⟨110⟩ directions aligned along the compression axis. Above this temperature, a combination of ⟨110⟩ and ⟨100⟩ textures was observed. Stout et al. [14] concluded, based on experimental observations and crystal plasticity simulations, that the ⟨100⟩ texture, which was a preexisting texture component, was retained at the elevated temperature due to a higher strain rate sensitivity and slip on the {110} planes that stabilized the initial cube orientation.

Crystal plasticity simulations have been used to better understand and predict the effect of additional active slip systems at elevated temperatures. In Stout et al. [14], the classical Taylor model is used [3], where each grain is assumed to undergo the macroscopic deformation. The simulations in Maurice and Driver [15] make use of a self-consistent model, see, for example, Molinari et al. [16], where each grain is treated as embedded in a homogeneous equivalent medium. More recently, in Ringeval et al. [13], a classical Taylor model is used and the resulting grain stresses are then modified by considering a weighted average of the stresses in neighboring grains. While these approaches provide useful predictions regarding texture evolution and macroscopic stress-strain response, they do not capture the intragrain heterogeneity.

In order to capture intragrain heterogeneity, discretized polycrystals, typically by the finite element method, can be considered. Idealized polycrystals with uniform grain shape have been considered. For example, in Beaudoin et al. [17], groups of brick elements in a uniform grid are distorted to form Wigner–Seitz cells, and in Dawson et al. [18] dodecahedral-shaped crystals are modeled. Other researchers have modeled polycrystals with discretizations composed of uniform brick elements, where groups of brick elements are defined as grains, see, for example, Sarma et al. [19]. Buchheit et al. [20] investigated the effect of mesh refinement in modeling 2.5D and 3D discretized polycrystals. They find that the stress and orientation distributions within grains are insensitive over a wide range of mesh densities, and that with sufficient subgrain mesh refinement, minor texture components, resulting from the breakup of grains with unstable orientations, are well predicted. While some aspects of the subgrain structure were not well captured, the characteristics of electron backscatter diffraction (EBSD) measured subgrain misorientation distributions were similar to the interelement misorientation distributions obtained from a polycrystal plasticity simulation when the same grid was used for the simulations as for the experiments.

In the present study, we apply an approach in which the grain structure is explicitly represented to investigate the response of a 6063 aluminum alloy at elevated temperatures. We focus on the effects that the additional active slip systems and increased rate sensitivity occurring at elevated temperatures have on the evolution of the grain structure, texture, and misorientations. This work utilizes a 17-grain, three-dimensional, representative polycrystal with smooth grain boundaries in which the grain size and shape distribution are consistent with the material of interest. A large number of finite elements (more than 1000) per crystal are used for the purpose of capturing the intragranular response and texture evolution. This discretization gives a similar resolution to EBSD measurements with a grid spacing of about 4–5 μm. To reduce the effect of boundary conditions, periodic boundary conditions are imposed on the model polycrystal. In order to investigate a larger number of orientations, simulations are performed considering three sets of representative orientations. Simulations allowing for only the 12 octahedral {111}⟨110⟩ slip systems are compared to those that consider the octahedral slip systems as well as slip on the additional 12 {110}⟨110⟩ and {001}⟨110⟩ slip systems. The model is calibrated against a macroscale compression test, and then the deformation history predicted by a macroscale simulation of the compression test is applied to the model polycrystals. The predicted microstructures, considering both 12 and 24 slip systems, are compared to the resulting grain structure from the compression test as well as observations reported in the literature. The experimental data are provided by Misiolek's group at Lehigh University, and similar compression test data on the same alloy are described in Ref. [21].

2 Multiscale Polycrystal Model Formulation

2.1 Grain Scale Model. First, we consider the behavior on the grain scale. Let us assume the motion $\mathbf{x}=\phi(\mathbf{X},t)$ and let $\mathbf{F}(\mathbf{X},t)=\nabla\phi(\mathbf{X},t)$ be the deformation gradient at the current time t and position $\mathbf{X}$ in the reference configuration Ω_0. The crystal elastoviscoplastic formulation is fairly standard and follows that given in Maniatty et al. [22] and is summarized here for completeness. A multiplicative decomposition of the deformation gradient into elastic and plastic parts, following the work of Lee [23], is assumed, where the elastic deformation gradient $\mathbf{F}^e$ can further be decomposed into the lattice rotation $\mathbf{R}^l$ and the elastic lattice stretch $\mathbf{U}^e$ by the right polar decomposition. We assume the plastic deformation gradient $\mathbf{F}^p$ is volume preserving and that crystallographic slip, accommodated by dislocation motion, is the only mechanism for plastic deformation so that

$$\hat{\mathbf{L}}^p = \dot{\mathbf{F}}^p \mathbf{F}^{p^{-1}} = \sum_{\alpha=1}^{N_s} \dot{\gamma}^\alpha \mathbf{P}^\alpha \tag{1}$$

where $\hat{\mathbf{L}}^p$ denotes the plastic velocity gradient on the relaxed configuration $\hat{\Omega}$, $\dot{\gamma}^\alpha$ is the rate of shearing on slip system α, N_s denotes the total number of slip systems for the crystal, and $\mathbf{P}^\alpha = \mathbf{s}^\alpha \otimes \mathbf{m}^\alpha$ is the Schmid tensor. Here, $\mathbf{s}^\alpha$ and $\mathbf{m}^\alpha$ denote the α slip direction and slip plane normal, respectively. For the elastic behavior, a linear relationship, with cubic symmetry, is assumed between the second Piola–Kirchhoff stress $\hat{\mathbf{S}}$ and the Green elastic strain $\hat{\mathbf{E}}^e$ on the relaxed configuration $\hat{\Omega}$.

To complete the constitutive model, it remains to relate the stress to the plastic deformation. This is accomplished by relating the resolved shear stress on a slip system τ^α to the rate of shearing on that slip system $\dot{\gamma}^\alpha$ through a usual power law. Specifically,

$$\dot{\gamma}^\alpha = \dot{\gamma}_o \frac{\tau^\alpha}{g^\alpha} \left| \frac{\tau^\alpha}{g^\alpha} \right|^{1/m-1} \tag{2}$$

where $\dot{\gamma}_o$ is a reference shear rate, m is the strain rate sensitivity, and g^α is the resistance to slip on the α slip system. The definition of the resistance to plastic slip (flow stress) on the slip systems g^α is described next.

As mentioned in Sec. 1, in addition to the 12 compact slip systems, slip is observed to occur on noncompact slip systems in aluminum alloys at the temperatures of interest. In particular, the family of six {001}⟨110⟩ slip systems and the family of six {110}⟨110⟩ slip systems are also available, giving a total of $N_s=24$ slip systems to consider. Based on the observations in Perocheau and Driver [9], we assume the resistance to slip on all the compact octahedral slip systems {111}⟨110⟩ is the same, i.e., $g^{\alpha_c}=g$, where α_c is a compact slip system. Likewise, on each of the noncompact slip system types, the flow stress is assumed to be the same and related to that on the compact slip systems using the ratios observed by Perocheau and Driver. It should be noted that these ratios were measured in a different aluminum alloy system,

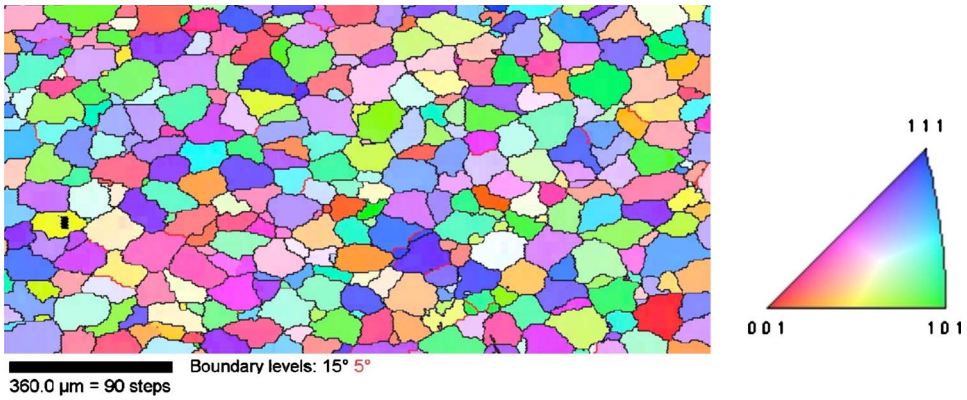

Fig. 1 Microstructure of cast and homogenized 6063 aluminum alloy prior to deformation. The image was colored using a [010] inverse-pole-figure color map, where [010] is the loading direction.

but in the absence of measurements for the alloy of interest, we take the same ratios. Specifically, for the $\{001\}\langle 110\rangle$ slip systems, we take $g^{\alpha_s}=1.4g$ and for the $\{110\}\langle 110\rangle$ slip systems, we take $g^{\alpha_p}=0.9g$, where α_s and α_p refer to each of the different types of noncompact slip systems. Now, only an evolution equation for the reference flow stress g is required. At the elevated temperatures of interest, the saturation flow stress, due to the simultaneous dislocation entanglement hardening and softening by recovery, is quickly reached after little hardening. A simple Voce–Kocks [24,25] type of hardening model is used to capture this phenomenon:

$$\dot{g} = G_o\left(\frac{g_s - g}{g_s - g_o}\right)\dot{\gamma} \tag{3}$$

$$\dot{\gamma} = \sum_{\alpha=1}^{24} |\dot{\gamma}^{\alpha}| \tag{4}$$

$$g_s = g_{s_o}\left|\frac{\dot{\gamma}}{\dot{\gamma}_s}\right|^{\omega} \tag{5}$$

where g_o is the initial reference flow stress, g_s is the saturation reference flow stress, and g_{s_o}, G_o, $\dot{\gamma}_s$, and ω are material parameters that need to be calibrated. The primary drawback of using this hardening model here is that it has no intrinsic length scale, so grain size and subgrain size effects are not captured. A model, such as that used in Beaudoin et al. [17], could capture such effects but is beyond the scope of the present work.

2.2 Macroscale-Grain Scale Link. In addition to the constitutive behavior linking the deformation history to the stress and evolution of material state, the usual equations of equilibrium must be satisfied and appropriate boundary conditions must be prescribed that represent as closely as possible the physical situation. In the present study, deformation at the grain scale is linked to the macroscale by way of a deformation gradient history recorded at an interior point of a macroscale finite element simulation. Specifically, the deformation history is imposed on a representative polycrystal through the boundary conditions, see, for example, work by Hill [26] and Miehe [27].

Periodic boundary conditions are applied on the representative polycrystal model to reduce boundary condition effects, where the experiment sample is assumed to be made by stacking identical polycrystal representative volume elements (RVEs) periodically. Here, a locally periodic, first order method is used. First order, locally periodic methods are appropriate if the material of interest is at an interior location, the microstructure is uniformly random (i.e., no gradient in the microstructure), and the deformation gradient can be treated as uniform in an average sense on the fine scale. These conditions hold here. The macroscale deformation gradient $\bar{\mathbf{F}}$ is treated as being constant over the fine scale, and the position of a material point on the fine scale is assumed to be governed by this deformation gradient plus a fluctuation field such that the spatial coordinates of a particle at the grain scale are given by

$$\mathbf{x} = \bar{\mathbf{F}}\mathbf{X} + \tilde{\mathbf{u}} \tag{6}$$

where $\tilde{\mathbf{u}}$ denotes the fluctuation in the displacement field on the mesoscale. Equilibrium is then achieved by permitting a fluctuation field, which can be solved for using the finite element method. The fluctuation field is periodic and must match on opposite sides of the RVE. Because of triple periodicity at the eight corners of the RVE (assuming a cubic RVE), the fluctuation field at the corners must be equal and is set to zero.

The above kinematic description together with the equilibrium equation and elastoviscoplastic crystal constitutive equations defines a boundary value problem on the grain scale for the fluctation field $\tilde{\mathbf{u}}$. Assuming a prescribed macroscopic deformation gradient, the boundary value problem can be solved using the finite element method.

2.3 Numerical Implementation. The constitutive equations described in Sec. 2.1 are integrated using the procedure described in Maniatty et al. [22] and implemented into a general purpose, parallelized finite element framework. A mixed formulation is used, where the increments of displacement fluctuation $\tilde{\mathbf{u}}$ and hydrostatic stress are interpolated separately to handle the nearly incompressible behavior at large strains. A consistent tangent is derived to ensure quadratic convergence in the solution of the resulting nonlinear system of equations. Details of the formulation can be found in Lu [28].

3 Polycrystal Model and Calibration

The 6063 aluminum alloy considered here to calibrate and test the polycrystal model is from a section of a billet that was cast with the direct-chill process, and then homogenized at 560°C for 4 h and cooled at a rate greater than 200°C/h. For more details about the processing and composition, see Van Geertruyden et al. [21]. The processing resulted in a fairly equiaxed grain structure with no strong texturing. Figures 1 and 2 were produced using data from an EBSD scan of the material before deformation. Figure 1 shows a projection of both the grain structure and the texture, as the grain orientations are colored according to the inverse-pole-figure color map shown. The area scanned is 800 $\times$ 1600 μm^2, and the step size is 4 μm. Figure 2 depicts the texture through an inverse pole figure. Looking at the scale bar, the

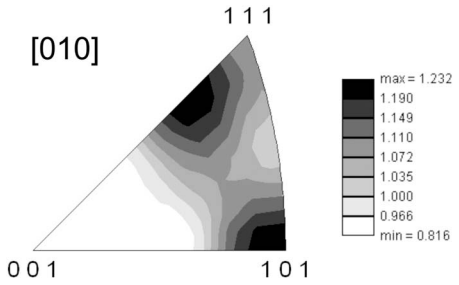

Fig. 2 Inverse pole figure showing texture for cast and homogenized 6063 aluminum alloy prior to deformation. The image is with respect to the [010] sample direction, where [010] is the loading direction.

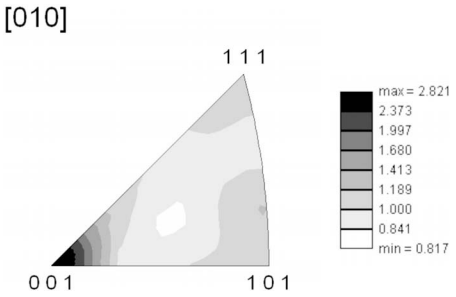

Fig. 4 Inverse pole figure made prior to deformation showing the composite set orientations used in the simulations. The [010] direction corresponds to the loading axis in the compression test.

texture appears fairly random with no strong texture components.

To mimic the observed initial grain structure in the polycrystal model, a three-dimensional polycrystal RVE was created using a modified Monte Carlo grain growth algorithm, following that presented in Radhakrishnan and Zacharia [29], and subsequent geometric modeling operations. This approach generates a model grain structure with equiaxed grains and a grain size distribution similar to that observed. The procedure for creating the representative polycrystal model is outlined below. A detailed treatment can be found in the thesis by Lu [28].

Creation of the polycrystal RVE involved three stages: grain growth using a modified Monte Carlo algorithm, extraction of topology information, and meshing. The grain growth algorithm operates on a regular structured grid, where each grid point is assigned an orientation, and groups of neighboring grid points with the same orientation define a grain. Here, a $50\times50\times50$ regular grid was used to define the RVE. In order to satisfy the periodicity assumption described in Sec. 2.2, periodic boundaries were created by linking opposite faces of the polycrystal RVE. A polycrystal with 17 grains (45 regions due to periodicity) was created. The Monte Carlo algorithm creates a voxel representation of the polycrystal RVE. To smooth the grain boundaries and allow for unstructured meshing for subsequent finite element analysis, a smooth geometric model was created from the voxel data. The smooth geometric model was generated by extracting topology information—vertices, edges, faces, and regions—from the voxel data. Finally, the polycrystal grain structure was meshed with 24,819 P2/P1 elements (tetrahedral elements, quadratic displacement interpolation, linear hydrostatic stress interpolation). While the grain structure is relatively small (only 17 grains), there is a good mesh resolution with on average about 1460 elements per grain to allow intragranular behavior to be studied. Grain orientations were assigned to the model polycrystal by sampling an experimentally obtained orientation distribution function. In order to partially compensate for the small number of grains in the polycrystal RVE, three sets of orientations were considered. The grain structure with the three sets of orientations is shown in Fig. 3 together with the inverse-pole-figure color map used to depict the orientations. An inverse pole figure showing the composite set of orientations considered is shown in Fig. 4. Since only 51 orientations are considered, the randomness of the initial texture is not well represented. While the sampling was random, a random sample that contained a preexisting ⟨100⟩ texture component was selected since the work of Stout et al. [14] observed that this texture component was stabilized at elevated temperatures.

The calibration work focused on determining the parameters in the constitutive model (namely, γ_o, m, G_o, g_o, g_{s_o}, $\dot{\gamma}_s$, and ω in Eqs. (2)–(5)) using available experimental results, which include a compression test performed at Lehigh by Misiolek's group and information in the literature. To narrow the scope of this work, and also due to the limited available data, only isothermal conditions were considered at a temperature of 482 °C, which is the test temperature of the compression test performed at Lehigh. The compression test was performed on a 15 mm long specimen with a 10 mm diameter that was produced as described at the beginning of Sec. 3. The test consisted of compression at 1 mm/s for 10 s to a final height of 5 mm (33% of the original height or a 67% reduction).

The calibration work consisted of two steps. First, an isotropic hardening model, analogous to that in Eqs. (3) and (4), was calibrated against the available stress-strain data from both literature and compression tests. Then, by matching the stress-strain curve of a polycrystal model under uniaxial tensile loading to the stress-strain curve generated by the calibrated isotropic hardening model, the polycrystal hardening model parameter values were determined. Different polycrystal models, made up of cube shaped grains, were used in producing the uniaxial tension stress-strain curve to ensure that the parameter values are model independent.

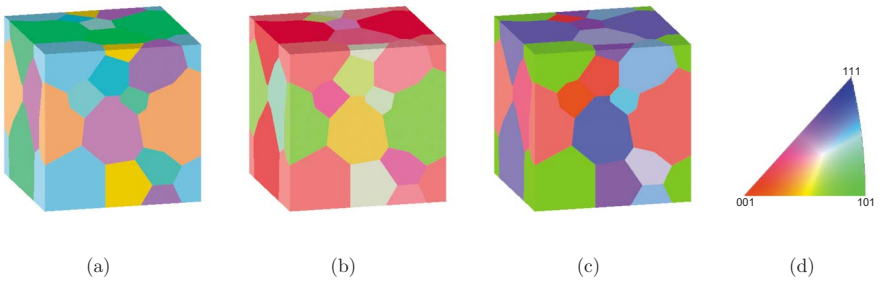

Fig. 3 Initial model grain structures. (*a*), (*b*), and (*c*) depict the three sets of orientations considered. The inverse-pole-figure color map is shown on the right and is with respect to the [010] sample direction (compression axis). The same color map is used for all simulation results.

Table 1 Calibrated hardening model parameters

Parameter	Value
$\dot{\gamma}_o$	3.0 s^{-1}
ω	0.0289
$\dot{\gamma}_s$	6.8634×10^{-8} s^{-1}
m	0.11
G_o	91.23 MPa
g_o	16.63 MPa
g_{s_o}	16.51 MPa

The final model parameters selected are given in Table 1. The elastic parameters for aluminum at 482°C, C_{11}=93.1 GPa, C_{12} =61.7 GPa, and C_{44}=21.0 GPa, were also used.

4 Numerical Results and Discussion

Before presenting the simulation results, we first present the experimental observations. The sample compression axis is the y axis ([010]). Figure 5 shows the resulting experimental grain structure near the center of the specimen and some of the local texture. Notice that there is a preponderance of red and purple and the color is nonuniform within the grains. Comparing Fig. 5 to the initial grain structure shown in Fig. 1, we see that the grains are more elongated and tend to have an orientation with the ⟨111⟩ or ⟨100⟩ direction along the transverse direction ([001]), and that the orientations within the grains are no longer uniform as depicted by the color variation within the grains. Figure 6 depicts the texture through inverse pole figures. Here, we also show the [010] inverse pole figure, which shows the texture developed along the compression axis. The highest texture components are ⟨110⟩ and ⟨100⟩, which is consistent with other experimental observations for aluminum alloys at elevated temperatures, see Stout et al. [14].

In the simulations, representative polycrystal models with the three sets of grain orientations considered were compressed to 60% of their original height using the deformation gradient history obtained from the macroscale compression simulation near the center of the specimen. This is not the total compression that was attained in the experiment and in the macroscale model, which was 33% of the initial specimen height, because the finite elements become too distorted to continue. For each grain structure, in order to see the effect of the additional sets of slip systems that become active at elevated temperatures, we ran cases with only the 12 compact, octahedral slip systems available as well as cases with all 24 slip systems available, using the same set of material parameters. Figure 7 shows the resulting inverse pole figures for the deformed grain structures comparing the cases with 12 slip systems with those allowing for 24 slip systems. Note that these inverse pole figures are with respect to the compression axis ([010]). We can see in Fig. 7(*a*) that when only 12 slip systems are considered the usual ⟨110⟩ texture component dominates, as expected. In Fig. 7(*b*), we see that the texture predicted with 24 slip systems still shows a dominant ⟨110⟩ texture, but a ⟨100⟩ component is also present. This is consistent with the observations in

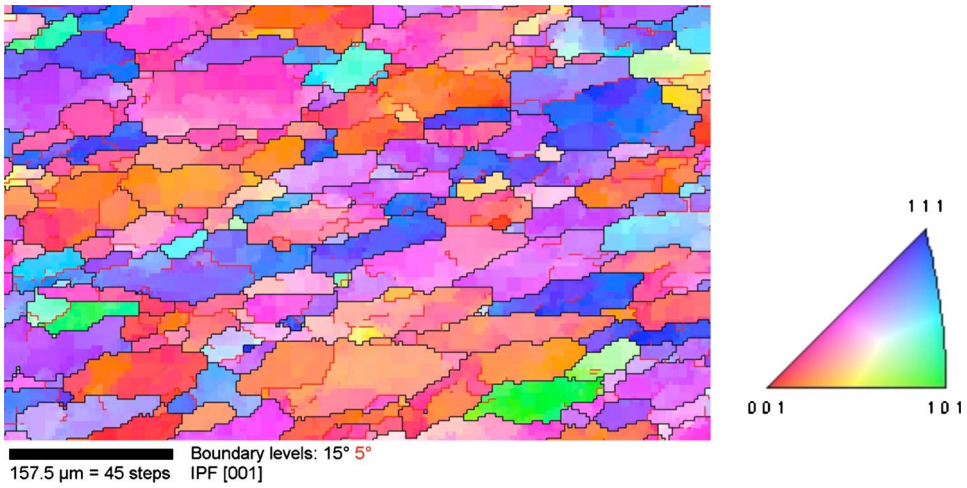

Fig. 5 Final microstructure of 6063 aluminum alloy subjected to uniaxial compression to a final height that is 33% of the initial height. EBSD scan is taken on material near the center of the specimen. The inverse-pole-figure color map is with respect to the [001] sample direction, which is a transverse direction ([010] is the compression axis).

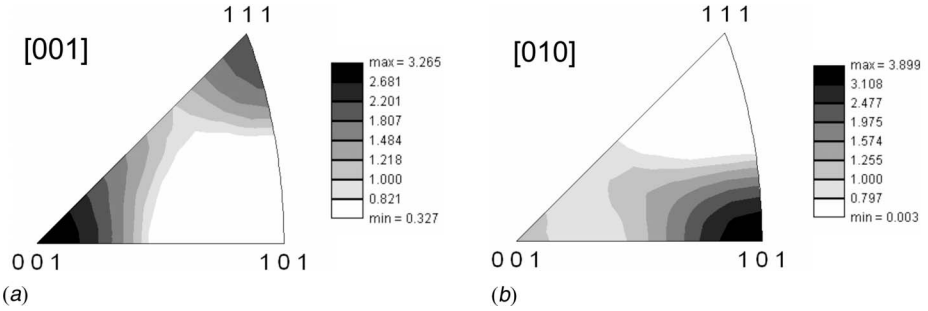

Fig. 6 Inverse pole figures showing texture of compressed 6063 aluminum alloy sample near the center of the specimen with respect to a transverse direction [001] and the compression direction [010].

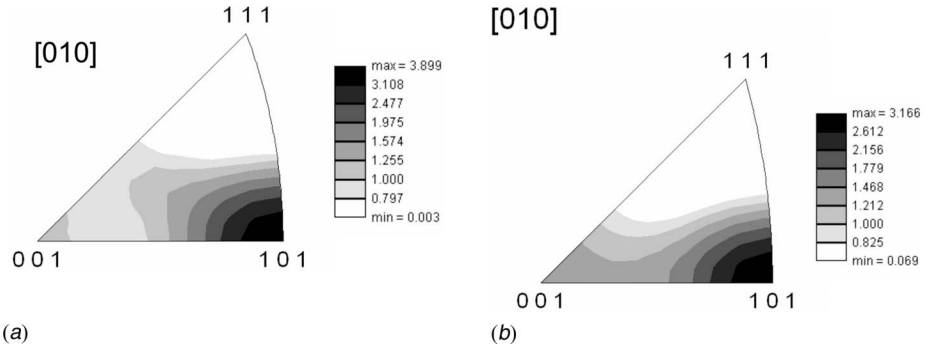

Fig. 7 [010] (compression axis) inverse pole figures showing predicted resulting textures where the results from all the three orientation sets are combined: (*a*) 12 slip system cases and (*b*) 24 slip system cases.

Stout et al. [14], who attributed the strong ⟨100⟩ final texture to a fairly strong initial cube texture that is stabilized by slip on the {110} planes.

Figures 8 and 9 show the resulting compressed grain structures allowing for 12 and 24 slip systems, respectively. The same [010] (compression axis) inverse-pole-figure color map used in Fig. 3 is used here to show the orientations. The periodicity of the deformed structures that was enforced through the boundary conditions is evident. Notice that the grains no longer have a uniform orientation, but the case allowing for 24 slip systems shows less orientation variability within the grains. It is also interesting to note that the deformation with 24 slip systems is considerably more uniform, which is not surprising given the additional deformation paths available. One way to quantify the nonuniformity of the deformation is to compute the average fluctuation in the displacement field from that of a uniform deformation. The average fluctuation in the displacement field for the 12 slip system cases is 2.4 times higher than that for the 24 slip system cases.

To make a more direct comparison to the experiment, we made a cut through the grain structures on an x-y plane in the interior of the grain structure (y is the compression axis) and show the before and after grain structures in Figs. 10–12. A rectangular region from within the cross section was used due to the restrictions of the imaging software. Figure 10 shows the original cross section considered with the initial orientations using the [010] inverse-pole-figure color map. Comparing Figs. 11 and 12, we see that the orientation variation within the grains appears to be greater for the 12 slip system case. To better show the orientation variation within the grains (misorientation), Fig. 13 shows the kernel average misorientation on a slice of the second orientation set comparing the case with 12 slip systems to that with 24 slip systems. The kernel average misorientation for a given point is the average misorientation between the point and all of its neighbors excluding misorientations greater than some prescribed value, 15 deg in this case, so as not to consider grain boundaries. In generating the results in Fig. 13, the kernel average misorientation was computed using the third nearest neighbors. We can see in these images that the case with 24 slip systems predicts lower typical misorientations over much of the cross section. These results are consistent with the observations described in Ringeval et al. [13], who observed that at elevated temperatures, the orientation distribution within grains is quite uniform. In addition, it is interesting to

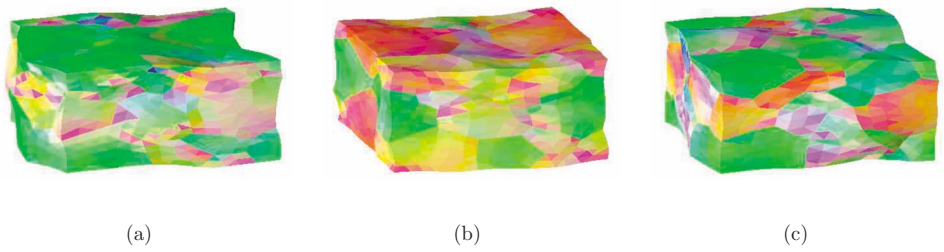

Fig. 8 Polycrystals compressed to 60% of their initial height with 12 slip systems available. (*a*), (*b*), and (*c*) are the three orientation sets considered. The inverse-pole-figure color map is with respect to the [010] sample compression axis.

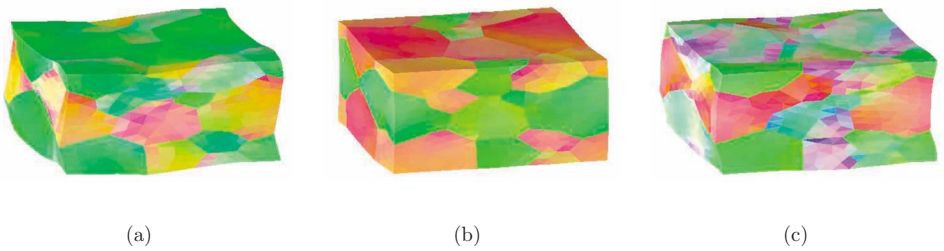

Fig. 9 Polycrystals compressed to 60% of their initial height with 24 slip systems available. (*a*), (*b*), and (*c*) are the three orientation sets considered. The inverse-pole-figure color map is with respect to the [010] sample compression axis.

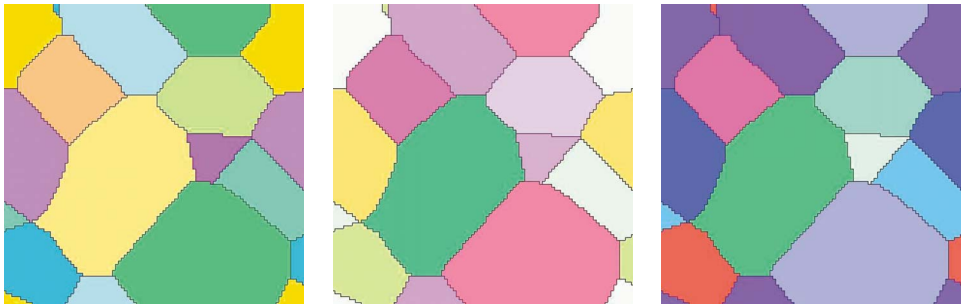

(a) (b) (c)

Fig. 10 Initial slice on an *x-y* plane for the three orientation sets considered. The inverse-pole-figure color map is with respect to the [010] sample compression axis.

investigate the distribution of misorientations. Following the procedure used in Dawson et al. [18], where the misorientations are computed across element boundaries, we compute the misorientation distributions for a single grain for both the 12 and 24 slip system cases. The result is shown in Fig. 14. Other grains were also investigated, with similar results, so only the single case is shown. Interestingly, the scaled distributions are very similar to each other and to those computed in Dawson et al. and those observed experimentally in Hughes et al. [6]. However, the average misorientations, used to scale these distributions, are quite different, with the average being 3.3 deg for the 12 slip system case and 1.84 deg for the 24 slip system case.

Finally, we investigate the slip system activity. Figure 15 shows the probability distribution for the number of active slip systems based on the model predictions for the 12 and 24 slip system cases. To define whether a slip system is active, we set a slip rate cutoff of 10^{-5} s^{-1}; if the slip rate is higher than this cutoff, the slip

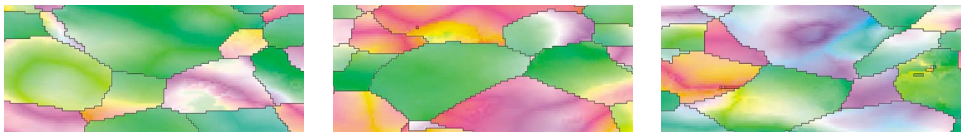

(a) (b) (c)

Fig. 11 Deformed slices on an *x-y* plane for cases allowing only 12 slip systems for the three orientation sets considered. The inverse-pole-figure color map is with respect to the [010] sample compression axis.

(a) (b) (c)

Fig. 12 Deformed slices on an *x-y* plane for cases allowing all 24 slip systems for the three orientation sets considered. Inverse-pole-figure color map is with respect to the [010] sample compression axis.

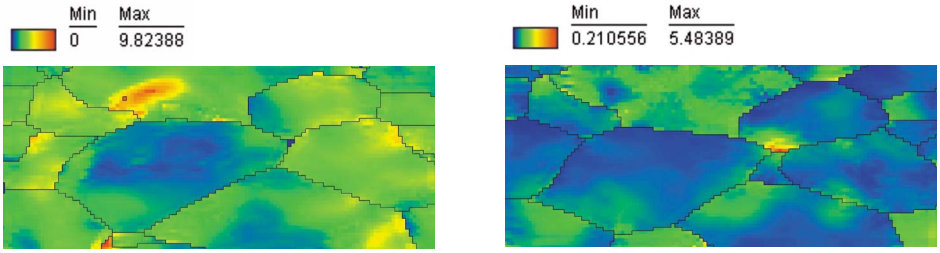

(a) (b)

Fig. 13 Deformed slice on an *x-y* plane showing the kernel average misorientation for the second orientation set. (*a*) 12 slip system case, (*b*) 24 slip system case.

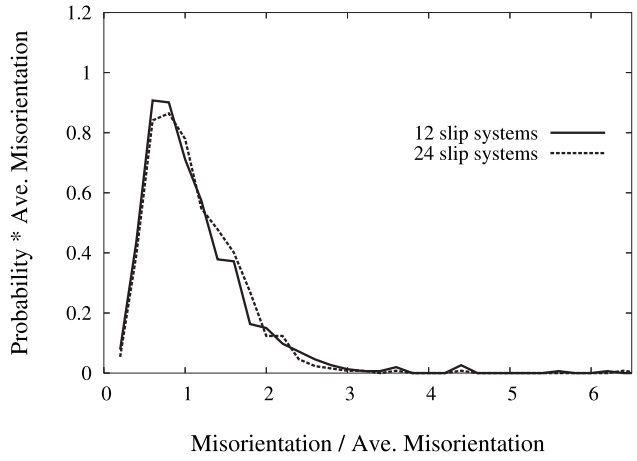

Fig. 14 Misorientation distributions within a single grain comparing the 12 slip system case with the 24 slip system case

system is considered active. Note that the macroscale strain rate is on the order of 0.1 s^{-1}. For the 12 slip system case, we see that the usual six or eight active slip systems make up 90% of the cases, which is not surprising. On the other hand, with 24 slip systems, we see a broader range for the number of active slip systems, with the highest probability being 10, 12, or 14 active slip systems, even though, like in the 12 slip system case, the rate independent yield surface of the 24 slip system case also has six or eight active slip systems at each vertex. The higher rate sensitivity, which rounds the corners of the flow surface, combined with the increased density of facets, i.e., there are more facets near a vertex than just those making up the vertex, leads to the higher number of active slip systems.

The results presented in Fig. 15 can be discussed in terms of several aspects of material behavior. Deformation tends to be very localized at cold temperatures, which is correlated with low rate sensitivity; at elevated temperatures, with a higher rate sensitivity, the deformation is more diffused (see, for example, Peirce et al. [5]). When the deformation is nonuniform within the grains, the requirement of at least five active slip systems for constrained grains is no longer necessary and, in fact, is frequently not observed. Furthermore, as observed in simulations by Maniatty and Yu [30], the number of active slip systems is also reduced by elastic effects, which continue to cause transients as the grains reorient and the stress state traverses the flow surface. However, at elevated temperatures, especially with additional slip systems available, the deformation within the grains is not as localized and is more uniform with higher numbers of active slip systems.

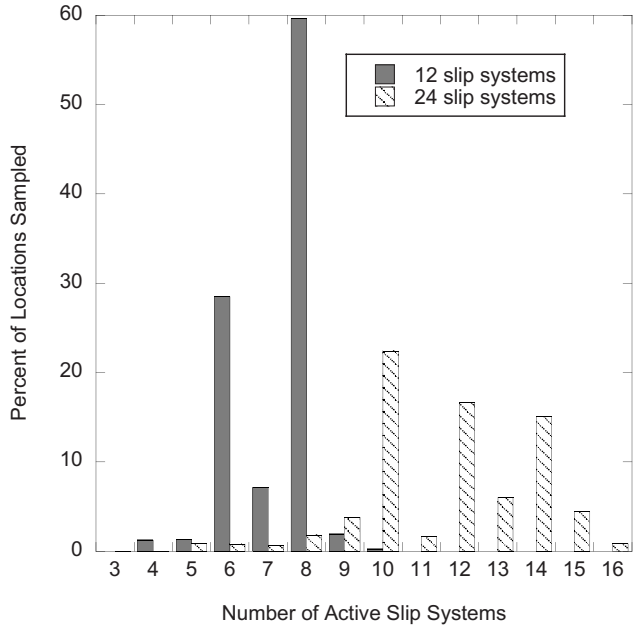

Fig. 15 Probability distribution showing predicted probability for a given number of slip systems for locations throughout the polycrystals at maximum compression for both the cases considering 12 slip systems and 24 slip systems

5 Conclusions

An overall framework for modeling representative polycrystal RVEs was presented with the model being specialized to consider an aluminum alloy at elevated temperatures. Specifically, a model that allows for both the usual octahedral $\{111\}\langle 110\rangle$ slip systems and the nonoctahedral $\{110\}\langle 110\rangle$ and $\{100\}\langle 110\rangle$ slip systems, which are active in aluminum alloys at elevated temperatures, is described. Simulation results considering only the 12 octahedral slip systems are compared to those allowing for all 24 slip systems, and the simulations are compared to experimentally observed microstructures resulting from a compression test conducted on a 6063 aluminum alloy. The simulations predict a more uniform deformation, and as a result, more uniform orientations within the grains, when 24 slip systems are available. This is consistent with the experimental observations reported in Ringeval et al. [13] and is not surprising given the additional deformation paths available. The higher strain rate sensitivity at elevated temperatures also contributes to the uniformity of the deformation. The texture predicted for the 24 slip system case is qualitatively similar to the experimental texture with both $\langle 110\rangle$ and $\langle 100\rangle$ texture components observed. While the average intragranular misorientation in the 12 slip system case was higher than that for the 24 slip system case, the scaled misorientation distributions for each case are similar. The number of active slip systems throughout the polycrystals was also recorded at maximum deformation allowing for the probability of a given number of active slip systems to be predicted. When 24 slip systems are allowed, the number of active slip systems (mostly in the range of 10–14) is usually larger than the number of slip systems when only 12 slip systems are available (typically 6 or 8).

The primary limitations of this work are the small grain structure considered, which is not sufficient to be truly representative, and the small number of orientations considered, which do not adequately represent the initial texture. The maximum deformation is also limited due to the element distortion. Modeling larger polycrystal structures with more grains and considering more set of orientations are topics of future work. Work is also being done to allow for remeshing so that larger deformations may be considered in the future.

Acknowledgment

This material is based upon work supported by the National Science Foundation under Grant Nos. DMI-0115146 and CMS-0502891. The Loewy Family Foundation also provided support through sponsoring A.M.M. as the Loewy Visiting Professor at Lehigh University in 2001. The authors thank W. Misiolek of Lehigh University for valuable discussions and for providing experimental data, A. Ingraffea and P. Wawrzynek of the Cornell Fracture Group for use of the FEMLIB software package, and F. Xu at Rensselaer Polytechnic Institute for generating most of the figures appearing in this paper.

References

[1] Olaf, E., and Hirsch, J., 2002, "Texture Control by Thermomechanical Processing of AA6xxx Al–Mg–Si Sheet Alloys for Automotive Applications—A Review," Mater. Sci. Eng., A, **A336**, pp. 249–262.
[2] Bay, B., Hansen, N., Hughes, D. A., and Kuhlmann-Wilsdorf, D., 1992,

"Overview No. 96: Evolution of F.C.C. Deformation Structures in Polyslip," Acta Metall. Mater., **40**, pp. 205–219.
[3] Taylor, G. I., 1938, "Plastic Strains in Metals," J. Inst. Met., **62**(1), pp. 307–324.
[4] Fleischer, R. L., 1987, "Number of Active Slip Systems in Polycrystalline Brass: Implications for Ductility in Other Structures," Acta Metall., **35**, pp. 2129–2136.
[5] Peirce, D., Asaro, R. J., and Needleman, A., 1983, "Material Rate Dependence and Localized Deformation in Crystalline Solids," Acta Metall., **31**, pp. 1951–1976.
[6] Hughes, D. A., Liu, Q., Chrzan, D. C., and Hansen, N., 1997, "Scaling of Microstructural Parameters: Misorientations of Deformation Induced Boundaries," Acta Mater., **45**, pp. 105–112.
[7] Hughes, D. A., and Hansen, N., 1997, "High Angle Boundaries Formed by Grain Subdivision Mechanisms," Acta Mater., **45**, pp. 3871–3886.
[8] Hughes, D. A., Chrzan, D. C., Liu, Q., and Hansen, N., 1998, "Scaling of Misorientation Angle Distributions," Phys. Rev. Lett., **81**, pp. 4664–4667.
[9] Perocheau, F., and Driver, J. H., 2002, "Slip System Rheology of Al-1%Mn Crystals Deformed by Hot Plane Strain Compression," Int. J. Plast., **18**, pp. 185–202.
[10] Kvapilová, M., and Orlová, A., 2002, "Traces of Non-Compact Glide in the Dislocation Structure of Copper after Creep at High Temperature," Mater. Sci. Eng., A, **A328**, pp. 277–282.
[11] Martin, J.-L., and Caillard, D., 1993, "The Importance of Non-Compact Slip in Some Close Packed Metallic Structures," Z. Metallkd., **84**(12), pp. 867–873.
[12] Maurice, C., and Driver, J. H., 1997, "Hot Rolling Textures of F.C.C. Metals—Part I. Experimental Results on Al Single and Polycrystals," Acta Mater., **45**(11), pp. 4627–4638.
[13] Ringeval, S., Piot, D., Desrayaud, C., and Driver, J. H., 2006, "Texture and Microstructure Development in an Al–3Mg–Sc(Zr) Alloy Deformed by Triaxial Forging," Acta Mater., **54**, pp. 3095–3105.
[14] Stout, M. G., Chen, S. R., Kocks, U. F., Schwartz, A. J., MacEwen, S. R., and Beaudoin, A. J., 1998, "Mechanisms Responsible for Texture Development in a 5182 Aluminum Alloy Deformed at Elevated Temperatures," Hot Deformation of Aluminum Alloys II, *Proceedings of TMS Symposium, Minerals, Metals & Materials Society*, Warrendale, PA, pp. 243–254.
[15] Maurice, C., and Driver, J. H., 1997, "Hot Rolling Textures of F.C.C. Metals—Part II. Numerical Simulations," Acta Mater., **45**(11), pp. 4639–4649.
[16] Molinari, A., Canova, G. R., and Ahzi, A., 1987, "A Self Consistent Approach of the Large Deformation Polycrystal Viscoplasticity," Acta Metall., **35**, pp. 2983–2994.
[17] Beaudoin, A. J., Acharya, A., Chen, S. R., Korzekwa, D. A., and Stout, M. G., 2000, "Consideration of Grain-Size Effect and Kinetics in the Plastic Deformation of Metal Polycrystals," Acta Mater., **48**, pp. 3409–3423.
[18] Dawson, P. R., Mika, D., and Barton, N., 2002, "Finite Element Modeling of Lattice Misorientations in Aluminum Polycrystals," Scr. Mater., **47**, pp. 713–717.
[19] Sarma, G. B., Radhakrishnan, B., and Zacharia, T., 1998, "Finite Element Simulations of Cold Deformation at the Mesoscale," Comput. Mater. Sci., **12**, pp. 105–122.
[20] Buchheit, T. E., Wellman, G. W., and Battaile, C. C., 2005, "Investigation the Limits of Polycrystal Plasticity Modeling," Int. J. Plast., **21**(2), pp. 221–249.
[21] Van Geertruyden, W. H., Claves, S. R., and Misiolek, W. Z., 2002, "Electron Backscatter Diffraction Analysis of Microstructural Evolution in Hot Deformed 6xxx Series Aluminum Alloys," Metall. Mater. Trans. A, **33A**, pp. 693–700.
[22] Maniatty, A. M., Dawson, P. R., and Lee, Y.-S., 1992, "A Time Integration Algorithm for Elasto-Viscoplastic Cubic Crystals Applied to Modeling Polycrystalline Deformation," Int. J. Numer. Methods Eng., **35**, pp. 1565–1588.
[23] Lee, E. H., 1969, "Elastic-Plastic Deformation at Finite Strain," ASME J. Appl. Mech., **36**, pp. 1–6.
[24] Voce, E., 1948, "A Practical Strain-Hardening Function," Acta Metall., **51**, pp. 219–226.
[25] Kocks, U. F., 1976, "Laws for Work-Hardening and Low-Temperature Creep," ASME J. Eng. Mater. Technol., **98**, pp. 76–85.
[26] Hill, R., 1985, "On the Micro-to-Macro Transition in Constitutive Analyses of Elastoplastic Response at Finite Strain," Math. Proc. Cambridge Philos. Soc., **98**, pp. 579–590.
[27] Miehe, C., 2003, "Computational Micro-to-Macro Transitions for Discretized Microstructures of Heterogeneous Materials at Finite Strains Based on the Minimization of Averaged Incremental Energy," Comput. Methods Appl. Mech. Eng., **192**, pp. 559–591.
[28] Lu, J., 2006, "Simulating Microstructure Evolution of Realistic 3D Aluminum Alloy Polycrystals during Large Plastic Deformation at Elevated Temperatures," Ph.D. thesis, Rensselaer Polytechnic Institute.
[29] Radhakrishnan, B., and Zacharia, T., 1995, "Simulation of Curvature-Driven Grain Growth by Using a Modified Monte Carlo Algorithm," Metall. Mater. Trans. A, **26**, pp. 167–180.
[30] Maniatty, A. M., and Yu, J.-S., 1996, "Effect of Elasticity on Slip System Activity in FCC Crystals: A Numerical Study," Int. J. Solids Struct., **33**, pp. 1069–1082.